https://doi.org/10.1016/j.electacta.2018.12.112

Enhancing the cycle life of Li-S batteries by designing a free-standing cathode with excellent flexible, conductive, and catalytic properties

Qian Lu [a1], Yang Sun [b1], Kaiming Liao [a,*], Xiaohong Zou [a], Ikutaro Hamada [b], Wei Zhou [a], Meng Ni [c], and Zongping Shao [a]

[a] State Key Laboratory of Materials-Oriented Chemical Engineering, College of Chemical Engineering, Nanjing Tech University, No. 30 South Puzu Road, Nanjing 211816, China

[b] Global Research Center for Environment and Energy based on Nanomaterials Science (GREEN), National Institute for Materials Science, 1-1 Namiki, Tsukuba 305-0044, Japan

[c] Department of Building and Real Estate, The Hong Kong Polytechnic University, Hung Hom, Kowloon, Hong Kong 999077, China

[1] Q. Lu and Y. Sun contributed equally to this work.

* Corresponding author

E-mail address: kaimingliao@njtech.edu.cn (K.M. Liao)

Abstract:

Poor electrical conductivity of sulfur, sluggish redox kinetics, dissolution of intermediate polysulfides, and expansion in volume upon cycling are the main drawbacks that hamper the practical application of Li-S batteries. By taking advantages of the high conductivity and favorable catalytic activity of RuO_2, we design a 3D carbon nanotube film with embedded RuO_2 nanoparticles as a freestanding type of chemisorptive and catalyst-like cathode for Li-S batteries, which can be facilely prepared by a surfactant-assisted vacuum infiltration method. Both experimental and theoretical results reveal the excellent capability of RuO_2 for anchoring polysulfides and accelerating the kinetics of polysulfides catalytic redox reactions. Besides, the 3D freestanding cathode is beneficial to overcoming pulverization during volume changes, especially for long-term cycling. At a high areal sulfur loading of 2 mg cm^{-2}, favorable initial capacities of 750 and 1060 mA h g^{-1} respectively at 2 and 0.5 C are achieved. More attractively, the capacity after 1000 cycles maintains 405 mA h g^{-1} at 0.5 C with a loss in capacity of only 0.06 % per cycle. Additionally, such freestanding cathode allows the batteries to be tested under various bending stages, hence encouraging more research works on fabrication of other 3D nanostructure families as high-performance cathodes for Li-S batteries.

Keyword: Lithium-sulfur battery; free-standing cathode; conductive network; chemical anchor; polysulfide redox kinetics.

1. Introduction

The ever-increasing demands from consumer electronics, electric vehicles, and grid-scale storage have stimulated intensive research activities on high-energy density batteries with low cost. Lithium-sulfur (Li-S) batteries, which are composed of "holy grail" anode of lithium metal and low cost cathode of sulfur, are regarded as a promising candidate for next-generation rechargeable battery systems owing to their high theoretical specific energy (1672 mA h g^{-1} based on reversible reaction of $2Li + S = Li_2S$), far exceeding that of Li-ion batteries (300 mA h g^{-1} based on graphite anodes and transition metal oxide cathodes). [1-4] However, there are some critical drawbacks that hamper the practical application of the now-established Li-S battery: (1) the conversion reaction of Li-ion and sulfur with the formation of Li_2S involves several soluble intermediate polysulfides (Li_2S_x, $4 \leq x \leq 8$), causing severe capacity fading and low coulombic efficiency; [5, 6] (2) both sulfur and the discharge product of Li_2S have poor electrical conductivity, leading to low utilization and sluggish reaction kinetics of sulfur; [7] (3) the reaction between sulfur and Li-ion with the formation of Li_2S undergoes about 80% expansion in volume, which may cause collapse of conductive framework and ultimately battery failure. [8] (4) the formation of mossy Li caused by inhomogeneous etching of the anode surface, leading to failure of Li-S batteries. [9]

To overcome the first drawback, many efforts have been devoted to confine the soluble polysulfides via physical adsorption and chemisorption, such as porous carbon nanostructures, [10-15] graphitic carbon nitride [16-18], metal oxides [19-29], perovskite oxides [30, 31], and metal sulfides [32-41]. However, some recent studies reveal that the physical and chemical adsorption materials may only alleviate the superficial problem of "shuttle effect" due to limited anchor sites. Recently, some catalyst-like materials [42-44] were found that can convert polysulfides to sulfur or Li_2S as soon as being adsorbed, thus providing reversible anchor sites for

polysulfides. [42, 44] Nevertheless, most metal oxides or sulfides are poor electronic conductors, which are hard to address the second drawback, resulting in sluggish redox kinetics for the conversion of the adsorbed polysulfides into sulfur or Li_2S. Of equal importance for Li-S batteries are the third drawback, which have leaded to cathode pulverization due to the volume change upon cycling. To solve the issue, 3D free-standing structure sulfur host exhibit the greatest potential in Li-S batteries. [45-47] Therefore, a new cathode capable of solving the multifaceted issues would be indispensable for practical application of Li-S batteries.

Herein, we report a 3D architecture by direct compositing RuO_2 nanoparticles within 3D CNTs structure with the formation of a porous RuO_2-embedded 3D CNTs film, and the freestanding cathode for Li-S batteries shows superior capacity, cycling stability and rate performance. Such 3D freestanding cathode with cross-linked configuration is not only important for overcoming pulverization during volume changes upon cycling, but also meaningful for designing flexible Li-S battery workable under harsh bending conditions. More importantly, the metallic RuO_2 (electronic conductivity ~10^4 S cm^{-1}) with hydrophilic nature performed as both an active site for the chemisorption of hydrophilic sulfur intermediates and a high-performance catalyst for promoting the reversible decomposition of polysulfides. A simple route based on the surfactant-assisted vacuum filtration was developed for the synthesis of RuO_2 nanoparticles decorated 3D CNTs film, thus served as an enabler for research efforts that devoted to high-performance Li-S battery.

2. Results and discussion

The synthesis procedure of flexible porous 3D CNTs@10%RuO_2 film is schematically shown in **Fig. 1a**. Here, SDBS (sodium dodecyl benzene sulphonate) as a surfactant was applied to assist the well dispersion of RuO_2 and CNTs in deionize water, while both RuO_2 nanoparticles and CNTs

are commercial products. The RuO_2 takes a rutile structure according to the X-ray diffraction (XRD) patterns as shown in **Fig. S1a**, and the particle size is in the range of 2-5 nm based on the HRTEM images in **Fig. S1b**. CNTs are multiwall in nature with the thickness of 2-15 nm and length of 13-15 μm. RuO_2 nanoparticles and CNTs were dropped into the SDBS solution in sequence under strong probe ultrasound sonication. The as-obtained ink-liked slurry was then vacuum filtrated to deposit onto a porous PVDF membrane. A freestanding 3D CNTs@10%RuO_2 film was obtained by peeling off the dried deposited layer from the surface of PVDF membrane. Such film was found to be highly flexible, demonstrating no crack formation after bending even at 180 ° (**Fig. 1b**), indicating its excellent flexibility and good mechanical strength.

The microstructure of the as-prepared 3D CNTs@10%RuO_2 film was first examined by scanning electron microscopy (SEM) from the top view (**Fig. 1c, S4a).** For comparison, the SEM image of the 3D CNTs film was also presented (**Fig. S4b**). The CNTs inside both films were well interconnected to form a three-dimensional conducting network. Thanks to the SDBS surfactant, no obvious aggregation of the CNTs was found, demonstrating the well dispersion of CNTs in the ink. **Fig. S5a**&**b** show the SEM images in lower magnification of the obtained 3D CNTs@10%RuO_2 film. The RuO_2 nanoparticles were evenly distributed inside the films without the appearance of large aggregates. To get further information about the distribution of RuO_2 nanoparticles inside the 3D CNTs@10%RuO_2 film, the element mapping of ruthenium, oxygen, and carbon distribution was conducted. As shown in **Fig. S4c**, elements of ruthenium and oxygen were uniformly distributed in the skeleton of the 3D CNTs@10%RuO_2 film. According to the cross-sectional SEM image and EDX in **Fig. 1d**, the 3D CNTs@10%RuO_2 film had a thickness of around 80 μm with homogeneous distribution of ruthenium and oxygen along the cross section as well. Based on the EDX analysis of a larger area of the film (**Fig. S6a, b**), the average contents of

C, Ru, and O were turned out to be 88.76, 8.70 and 2.54 *wt*%, respectively. It also suggests the atom ratio of Ru and O are around 1:2, in well agreement with the atom ratio of Ru and O in RuO_2, indicating the RuO_2 nature of Ru in the film. The content of RuO_2 was calculated to be around 10 *wt*%, in consistence with the set ratio during the preparation.

Active sites for polysulfides chemisorption was introduced on cathode surface, and widely adopted to suppress the shuttle effect in Li-S batteries. The adsorption capability of RuO_2 for polysulfides was first experimentally examined through ex-situ UV-vis spectroscopy with Li_2S_6 as the representive polysulfide. For comparison, the capability of CNTs and g-C_3N_4 for the adsorption of polysulfide was also studied. The adosprtion of Li_2S_6 from the solution over the absorbent will cause a change in the concentration of Li_2S_6 in the solution, which can be monitored by UV-vis spectroscopy. The specific surface area of RuO_2, g-C_3N_4 and CNTs is 206, 118, and 265 m^2 g^{-1}, respectively. To exclude the physical adsorption of polysulfides, the absolute surface area of the three samples kept at the same by controlling the amount of materials used during the testification based on UV-vis spectroscopy.

In **Fig. 2a**, strong absorbance in the range of 400~450 nm was clearly observed for pure Li_2S_6 solution (2.5 mM), agreeing well with previous reports. [39, 48] After the immersion of CNTs into the Li_2S_6 solution, slightly reduced absorbance in the range of 400~450 nm as compared with the pure Li_2S_6 solution was observed, attributing to physico-adsorption of partial Li_2S_6 over the surface of CNTs. In contrast, after immersing the solution with proper amount of RuO_2 of with equal surface area to CNTs, the UV-vis absorbance in the range of 400~450 nm was totally disappeared, suggesting the complete adsorption of Li_2S_6 over the surface of RuO_2. Correspondingly, the color of the Li_2S_6 solution (inset in **Fig. 2a**) became almost colorless after the exposure to RuO_2, while

it is still in a deep orange color for the Li_2S_6 solution after exposed to CNTs. Above results strongly suggest the much better adsorption capability of RuO_2 than CNTs for Li_2S_6.

It was reported that g-C_3N_4 is also an excellent absorbent for the chemical adsorption of polysulfides. [16-18] Based on the experiments of different concentrations of Li_2S_6 solution (16 mL, 5 mM and 20 mM, equaled to 1.5 mg and 6.1 mg sulfur, respectively) and the same surface area of RuO_2 nanoparticles and g-C_3N_4 (5 mg RuO_2 and 9 mg g-C_3N_4), RuO_2 showed even better Li_2S_6 adsorption capability than g-C_3N_4. As shown in **Fig. S9**, when the concentration of Li_2S_6 is 20 mM, the red brown Li_2S_6 solution turned to transparent solution after exposed to RuO_2 nanoparticles, suggesting the full adsorption of Li_2S_6 over the RuO_2 surface, while the Li_2S_6 solution could not be fully adsorbed over the g-C_3N_4 surface, as indicated by the unchanged color of the Li_2S_6 solution after the immersion with g-C_3N_4 of same surface area to RuO_2.

Li_2S_6 was used as polysulfide species to directly probe the adsorption state on the surface of RuO_2. It was reported that the chemical adsorption of Li_2S_6 over g-C_3N_4 surface was realized via the formation of Li-N bond. [12, 13] The chemical interaction of RuO_2 nanoparticles with Li_2S_6 was first analyzed by X-ray photoelectron spectroscopy (XPS). **Fig. 2b** displays the XPS S2p spectra of pristine Li_2S_6 and the Li_2S_6 after exposed to RuO_2 nanoparticles. The upper profile in **Fig. 2b** shows two $S2p_{3/2}$ contributions at 161.4 and 163.0 eV, which were assigned to the terminal sulfur (S_T^{-1}) and bridging sulfur (S_B^0), respectively. [19, 26] After impregnating Li_2S_6 onto the surface of RuO_2, the XPS S2p spectra became different. New Ru-S bond located at 162.4 eV was appeared, in well agreement with previous reports.[49-51] As to the XPS S2p spectra of 3D CNTs@Li_2S_6, the peaks at 164.0 eV was appeared, attributed to weak S^0-C, formed from weak physical adsorption of sulfur over the surface of carbon nanotube (**Fig. S10a**).[26] In addition, polythionate complex (167.2 eV) and sulfite (166.1 eV) were appeared, caused by the

crystallization water over the surface of RuO_2 nanoparticles.[19] The XPS Li 1s spectra of Li_2S_6 and RuO_2@Li_2S_6 were also presented in **Fig. 2c**. The Li 1s that contributed at 55.2 eV corresponded to the bond between S and Li in Li_2S_6. [16, 53] The CNTs@Li_2S_6 shows the similar spectra of Li 1s (**Fig. S10b**). In contrast, the XPS Li 1s spectra of RuO_2@Li_2S_6 contributions at 55.2 and 54.2 eV corresponded to the Li-S bond in Li_2S_6 and Li-O bond formed between Li in Li_2S_6 and O in RuO_2, respectively. [16, 53, 54] To further confirm the formation of Ru-S bond, Fig. 3d shows the XPS Ru $3d_{5/2}$ spectra of rutile RuO_2. The content of Ru^{3+} was found to be higher than Ru^{4+} in the near surface. After the adsorption of Li_2S_6 on the surface of RuO_2, the XPS Ru $3d_{5/2}$ spectra was mainly composed of the Ru-S bond. [49] Meanwhile, the content of Ru^{3+} species sharp declined. It suggests the Ru-S bond was arose from under-coordinated Ru atoms on the surface.

Density functional theory (DFT) calculations were performed to understand the role of RuO_2 nanoparticles in the Li-S electrochemistry. The RuO_2 (110) surface, which have been investigated extensively in catalytic reactions, was adopted to study the adsorption of lithium polysulfides occurred in Li-S batteries (**Fig. S11**). [55] For comparison, the adsorption energies of both graphene (a substitution model for CNTs for simplicity) and g-C_3N_4 were also calculated (**Fig. S12**). The optimized geometries of absorbed Li_2S_n (n = 4, 6, 8) are displayed in **Fig. S13**. Compared with the non-bonded graphite and Li-N bonded g-C_3N_4 (**Fig. 3a, b)**, our results unambiguously demonstrate that Li polysulfides were adsorbed on the RuO_2 surface by forming both Li-O and Ru-S bonds, consistent with the above results of XPS. The formation of strong chemical bonds between Li sulfides and RuO_2 surface can be visualized by the charge density difference (**Fig. 3c)**. Significant charge transfer can be seen, unambiguously demonstrating the strong chemical bonds after adsorption and rationalizing the large calculated adsorption energy. The Li-O bond formed

on the RuO_2 surface is analogous to lithium bonds reported elsewhere. [30] The Ru-S bond arises from under-coordinated Ru atoms on the surface. The surface Ru atoms receive extra electrons from the Li polysulfide, which may explain the aforementioned change in XPS Ru $3d_{5/2}$ spectra. The calculation results well support the conclusion based on the XPS analysis.

Fig. 3e show the calculated adsorption energies of Li polysulfides on the surfaces of carbon, g-C_3N_4 and RuO_2, respectively. Among them, the RuO_2 surface shows the largest value due to the coexistence of both lithium and sulfur bonds, rationalizing the excellent performance of RuO_2 nanoparticles in our experiment. To evaluate the possibility of reutilizing adsorbed Li polysulfides, we further calculated the delithiation voltage of lithium polysulfides after being adsorbed on surfaces of both g-C_3N_4 and RuO_2. For both g-C_3N_4 and RuO_2 surfaces, the voltage required to extract lithium from the adsorbed lithium polysulfides is lower than the thermodynamic equilibrium voltage of Li-S batteries ($2Li + S \leftrightarrow Li_2S$), as shown in **Fig. 3f**. It should be noted, however, that good electronic conductivity is another prerequisite for the delithiation reactions. In this sense, RuO_2 nanoparticles with high electronic conductivity enable a facile utilization of adsorbed compared with the g-C_3N_4. Given the dual role of RuO_2 in stabilizing and reutilizing lithium polysulfides, we may reasonably expect a much superior electrochemical performance by integrating RuO_2 nanoparticles into Li-S batteries.

Considering the solubility of polysulfides in electrolyte, the catalytic conversion of chemically adsorbed polysulfides to S or Li_2S will further contribute to suppressed shuttle effect of polysulfides, beneficial for cycling stability. [43, 44] Then cyclic voltammetry was used to analyze the catalytic performance of RuO_2 for the decomposition of polysulfides. **Fig. 4a** shows the cyclic voltammetries of 3D CNTs@10%RuO_2 and 3D CNTs cathodes for the first cycle between 1.7 and 2.8 V. The 3D CNTs@10%RuO_2 shows two peaks of discharge located at 2.198 and 1.998 V at

first cycle, corresponding to the formation of higher-order Li_2S_n ($4 \leqslant n \leqslant 8$) and lower-order Li_2S_n ($1 \leqslant n \leqslant 3$), respectively, which is similar to the 3D CNTs electrode. As to the charging process, the 3D CNTs@10%RuO_2 electrode shows two peaks located at 2.356 and 2.412 V, and the position of peaks shift to left about 0.024 and 0.036 V respectively as compared to the 3D CNTs electrode (2.380 and 2.448 V). [5, 41] The large polarization of discharge was caused by the uneven distribution of sulfur after the reduction of Li_2S_6 to sulfur. The lower polarization of the 3D CNTs@10%RuO_2 electrode illustrates the more steady deposition of sulfur. In **Fig. S14a, b**, after eight cycles, the peaks position of the 3D CNTs@10%RuO_2 electrode shifted to 2.325 and 2.422 V, respectively. Compared to 2.349 and 2.450 V of the 3D CNTs electrode, the lower charging voltage plateau ascribed to the catalytic activity of RuO_2 for polysulfides. To further elucidate the catalytic effects, **Fig. 4b** shows the cyclic voltammetry (CV) curves at 50 mV s^{-1} within the voltage window of -0.8 to 0.8 V, and the promotion of polysulfides conversion was directly confirmed by CV in symmetric cells employing 3D CNTs@10%RuO_2 or 3D CNTs as the electrodes in 0.5M Li_2S_6 electrolyte. The increased redox current density in the Li_2S_6-containing cell with the 3D CNTs@10%RuO_2 electrode can be ascribed to the fast redox reaction kinetics of Li_2S_6 on the conductive RuO_2 nanoparticles. The symmetric cell test indicated that RuO_2, with a multiple adsorptive capability toward polysulfides, can serve as an activator to trigger a rapid polysulfides conversion in the Li-S redox reactions. [29, 30, 43]

The electrochemical performance of the 3D CNTs@10%RuO_2 film as a freestanding cathode in Li-S battery was also studied by galvanostatic cycling under different rates, and comparison was made with batteries built from the 3D CNTs, 3D CNTs@10%C_3N_4 cathodes. As shown in **Fig. 4c**, the 3D CNTs@10%RuO_2 cathode displayed average discharge capacities of 1150, 910, 805 and 750 mA h g^{-1} at the discharge current densities of 0.2, 0.5, 1 and 2 C, respectively. As a comparison,

the 3D CNTs cathode shows much lower discharge capacities of 875, 690, 645 and 620 mA h g^{-1} at the discharge current densities of 0.2, 0.5, 1 and 2 C, respectively. It suggests the introduction of RuO_2 into the cathode significantly improved the rate performance. After the cycling at various rates for 20 cycles, a reversible average discharge capacity of 985 mAh g^{-1} was still retained at 0.2 C for the 3D CNTs@RuO_2 electrode. As well, a stable capacity was maintained cycling at the constant current density of 0.2 C, suggesting the superior cycling stability of the 3D CNTs@RuO_2 freestanding electrode in Li-S battery.

By taking 985 mAh g^{-1} as the stable reversible capacity at 0.2 C, a capacity retention of 75.5% was achieved when the discharge rate increased 10 times to 2 C, indicating the outstanding rate performance. Such high rate performance is closely related to the high catalytic activity of RuO_2 for decomposition of polysulfides, as well as good charge transfer capability for the metallic behavior of RuO_2. As it is well known, both S and Li_2S are insulators, while the electrode reaction involves charge transfer, a poor electronic conductivity of polysulfides absorbent may impede the electrode reaction, thus resulting in poor rate performance. To emphasize the important role of electronic conductivity of polysulfides absorbent for enhancing rate performance, a Li-S battery with the 3D CNTs@10%C_3N_4 film as the freestanding cathode was also comparatively studied at different rates. Although a high discharge capacity of 1070 mA h g^{-1} was achieved at 0.2 C, the capacity reduced quickly to only 801 mA h g^{-1} at 0.5 C and 525 mAh g^{-1} at 2 C, respectively. Considering the reversible average discharge capacity of 932 mAh g^{-1} at 0.2 C, the capacity retention at 2 C is only 56.3 % for the 3D CNTs@10%C_3N_4 electrode, as a comparison of 75.5 % for the 3D CNTs@10%RuO_2 electrode. Clearly, the metallic behavior and semiconductor behavior respectively of RuO_2 and g-C_3N_4 contributed to the main difference in their rate performance.

Fig. S15 shows the first discharge/charge curve of the 3D CNTs@10%RuO_2, 3D CNTs@10%C_3N_4 and the 3D CNTs electrodes at 0.2 C. The electrodes were first charged to allow the conversion of Li_2S_6 into elemental sulfur. All three electrodes demonstrated the same capacity of about 200 mA h g^{-1}, corresponding to the conversion of Li_2S_6 into elemental sulfur. However, the 3D CNTs@10%RuO_2 showed the lower charge potential platform, this further confirmed the better catalytic activity for the Li_2S_6 decomposition. The 3D CNTs@10%RuO_2 electrode not only showed the higher discharge capacity, but also the lower charge plateau than the 3D CNTs film electrode. **Fig. 4d** and **S16a, b** show the first discharge/charge curve at various current densities of the three electrodes, the 3D CNTs@10%RuO_2 electrode shows lower polarization resistance especially at high current densities than the other two electrodes, owing to the excellent conductibility of RuO_2.

Galvanostatic charge/discharge was performed to evaluate the cycling performance of the pristine 3D CNTs, 3D CNTs@10%C_3N_4, and 3D CNTs@10%RuO_2 electrodes with the same amount of Li_2S_6. As displayed in **Fig. 4e,** the three electrodes show similar cycling stabilities at the initial 100 cycles. However, the 3D CNTs and 3D CNTs@10%C_3N_4 electrodes both demonstrate sharp decrease of capacities and Coulombic efficiency with further decrease in cycling times. This may be related to the lacking of chemical anchor sites on the pristine 3D CNTs electrode as well as the poor electronic conductibility of the g-C_3N_4 electrode, both led to obvious "shuttle effect". Therefore, alleviating the "shuttle effect" of Li-S battery should both cover the two points about anchoring the polysulfides and transporting electrons. Fortunately, the freestanding metallic RuO_2 decorated 3D CNTs film provides great potential to address these issues. As shown in **Fig. 4e, f**, the 3D CNTs@10% RuO_2 electrode demonstrated good cycling stabilities at both low and high galvanostatic charge/discharge rates. At high areal sulfur loading

of 2 mg cm^{-2}, the initial capacities of the 3D CNTs@10%RuO_2 electrode reached 750 and 1060 mA h g^{-1} at a rate of 2.0 and 0.5 C, respectively. The capacity after 1000 cycles maintains 405 mA h g^{-1} at a rate of 0.5 C, corresponding to a loss of only 0.06% in each cycle and indicating the excellent cycle stability.

To take the advantage of the bendable nature of the 3D CNTs@10%RuO_2 film, a flexible soft packaging Li-S battery was also fabricated through sealed vacuum thermal sealing machine. As schematically illustrated in **Fig. 5a**, freestanding 3D CNTs@10%RuO_2 film fixed on aluminum tab-lead, Celgard 2400, and lithium foil attached with nickel tab-lead and copper foil were used as cathode, electrolyte and anode, respectively. The aluminum-plastic film was employed to pack these components. The digital photo of the assembled flexible Li-S battery is shown in **Fig. 5b**, from which the OCV of 2.35 V was achieved. To assess the flexibility of Li-S batteries with the freestanding 3D CNTs@10%RuO_2 electrode, different bending conditions was applied upon cycling. As show in **Fig. 5c** are the charge-discharge curves of flexible Li-S battery at various bending angles (0, 90, and 120 °) for the first and 5th cycle, which show the typical charge-discharge curves of Li-S batteries. The cycling performance of the flexible Li-S battery was also given in **Fig. 5d**, the average capacity under the flat condition reached 1115 mAh g^{-1}, and the average capacity retained at 983 and 930 mAh g^{-1} under bending conditions of 90 and 120 °, respectively. After recovering to flat status, a reversible average discharge capacity of 1014 mAh g^{-1} was still retained. Corresponding photographs of bending conditions were also given in the Fig. 5d. Furthermore, the flexible Li-S battery successfully lighted up a yellow LED under different bending conditions (**Fig. S17**), all of that suggesting the potential application in flexible and wearable electronic devices.

The remarkable cycling stability and rate performance of the Li-S battery with the freestanding 3D CNTs@10%RuO_2 host could be attributed to the presence of synergistic effect between polysulfides anchoring and electron transferring, as shown in **Fig. 6a, b**. On the one hand, the effective physico-sorption was achieved due to the high surface area of the 3D CNTs (~260 m^2 g^{-1}). More importantly, the strong chemical interaction between polysulfides and polar RuO_2 was realized by forming double cross-linked S-Ru and Li-O bonds based on the Lewis acid-base theory. The S-Ru bond arose from under-coordinated Ru atoms on the surface. The surface Ru atoms with empty orbitals received extra electrons from the Li polysulfides. Meanwhile, the Li-O bond established through negative O atoms with additional lone pair electrons. The terminal lithium atoms in polysulfides received extra electrons. Therefore, the shuttle of polysulfides was effectively suppressed. On the other hand, the superior electrical conductivity of 3D CNTs and metallic RuO_2 (2×10^4 S cm^{-1}) provided a conductive network for electrons transport freely within the whole electrode, thus contributing to good rate performances.[56, 57] Furthermore, RuO_2 served as a catalyst for the transformation of polysulfides to sulfur or Li_2S as soon as being adsorbed, which effectively provided "recyclable" anchor sites for more polysulfides, thus benefiting for alleviation of shuttle effect, especially with a high areal mass loading of sulfur on the cathode.

3. Conclusions

In summary, flexible freestanding 3D CNTs@10%RuO_2 film with closely linked 3D CNTs architecture was successfully prepared by a facile vacuum filtration method. By using as a novel host material for Li-S battery, excellent performance, including capacity, rate capability and cycling stability, was achieved. The as-prepared 3D CNTs@10%RuO_2 electrode with high sulfur loading of about 2 mg cm^{-1} delivered attractive discharge capacities of 1325 and 750 mA h g^{-1} at

0.2 and 2 C, respectively. At 1 C, a capacity of 660 mA h g^{-1} was retained after 400 cycles, higher than 181 mA h g^{-1} of the 3D CNTs film electrode and 161 mA h g^{-1} of 3D CNTs@10%C_3N_4 film electrode, and the decay rate was only 0.06 % per cycle at 0.5 C for the 3D CNTs@10%RuO_2 electrode during long cycling test. The 3D CNTs@10%RuO_2 electrode demonstrated a significantly higher electrochemical performance than the unmodified 3D CNTs electrode and the modified 3D CNTs@10%C_3N_4 electrode, including higher cycling stabilities and better rate capabilities. All that indicate RuO_2 nanoparticles played a key role in the superior performance of Li-S battery. The attractive performance is related to the superior adsorption capability of RuO_2 for Li_2S_6, good electronic conductivity and high catalytic activity for polysulfides redox reactions, as well as cross-linked 3D configuration to overcome pulverization upon cycling. This study provides a new polar and conductive metal oxide embedded in 3D CNTs film to trap polysulfide, overcome cathode pulverization, and accelerate the redox kinetics in Li-S battery. The results should encourage more research studies on 3D freestanding architectures loading with polar and conductive materials to achieve the Li-S batteries with long lifespan.

Acknowledgements

This work was financially supported by National Natural Science Foundation of China (No. 51802152), Natural Science Foundation of Jiangsu Province of China (No. BK20170974), Jiangsu Natural Science Foundation for Distinguished Young Scholars (No. BK20170043), and Ministry of Education, Culture, Sports, Science and Technology, Japan through the "Development of Environmental Technology using Nanotechnology" program. The numerical calculations were performed using the Numerical Materials simulator of National Institute for Materials Science.

Appendix A. Supplementary material

Supplementary data associated with this article can be found in the online version at xxxxxx.

References

[1] A. Manthiram, Y.Q. Fu, Y.-S. Su, Challenges and Prospects of Lithium-Sulfur Batteries, Acc. Chem. Res. 46 (2013) 1125–1134.

[2] R. Xu, J. Lu, K. Amine, Progress in Mechanistic Understanding and Characterization Techniques of Li-S Batteries, Adv. Energy Mater. 5 (2015) 1500408.

[3] K. Liao, S. Wu, X. Mu, Q. Lu, M. Han, P. He, Z. Shao, H. Zhou, Developing a "Water-Defendable" and "Dendrite-Free" Lithium-Metal Anode Using a Simple and Promising $GeCl_4$ Pretreatment Method, Adv. Mater. 30 (2018) 1705711.

[4] X. Zou, Q. Lu, Y. Zhong, K. Liao, W. Zhou, Z. Shao, Flexible, Flame-Resistant, and Dendrite-Impermeable Gel-Polymer Electrolyte for Li–O_2/Air Batteries Workable Under Hurdle Conditions, Small 14 (2018) 1801798

[5] Y.X. Yin, S. Xin, Y.G. Guo, L.J. Wan, Lithium–Sulfur Batteries: Electrochemistry, Materials, and Prospects, Angew. Chem. 52 (2013) 13186-13200.

[6] S. Evers, L. F. Nazar, New Approaches for High Energy Density Lithium-Sulfur Battery Cathodes Acc. Chem. Res. 46 (2013) 1135-1143.

[7] Y. Yang, G. Zheng, Y. Cui, Nanostructured sulfur cathodes, Chem. Soc. Rev. 42 (2013) 3018-3032.

[8] A. Manthiram, S.H. Chung, C. Zu, Lithium–Sulfur Batteries: Progress and Prospects, Adv. Mater. 27 (2015) 1980-2006.

[9] Y. Zhang, F.M. Heim, N. Song, J.L. Bartlett, X. Li, New Insights into Mossy Li Induced Anode Degradation and Its Formation Mechanism in Li−S Batteries, ACS Energy Lett. 2 (2017) 2696−2705.

[10] Y. Zhong, S. Wang, Y. Sha, M. Liu, R. Cai, L. Li, Z. Shao, Trapping sulfur in hierarchically porous, hollow indented carbon spheres: a high-performance cathode for lithium–sulfur batteries, J. Mater. Chem. A 4 (2016) 9526-9535.

[11] Q. Lu, Y. Zhong, W. Zhou, K. Liao, Z. Shao, Dodecylamine-Induced Synthesis of a Nitrogen-Doped Carbon Comb for Advanced Lithium–Sulfur Battery Cathodes, Adv. Mater. Interfaces 5 (2018) 1701659.
[12] T.-Z. Hou, X. Chen, H.-J. Peng, J.-Q. Huang, B.-Q. Li, Q. Zhang, B. Li, Design Principles for Heteroatom-Doped Nanocarbon to Achieve Strong Anchoring of Polysulfides for Lithium–Sulfur Batteries, Small 12 (2016) 3283-3291.
[13] Z. Gao, Y. Zhang, N. Song, X. Li, Biomass-derived renewable carbon materials for electrochemical energy storage, Mater. Res. Lett. 5 (2017) 69–88.
[14] Y. Zhang, Z. Gao, N. Song, J. He, X. Li, Graphene and its derivatives in lithiumesulfur batteries, Mater. Today Energy 9 (2018) 319-335.
[15] Y. Zhong, Q. Lu, Y. Zhu, Y. Zhu, W. Zhou, S. Wang, Z. Shao, Fructose-Derived Hollow Carbon Nanospheres with Ultrathin and Ordered Mesoporous Shells as Cathodes in Lithium–Sulfur Batteries for Fast Energy Storage, Adv. Sustainable Syst. 1 (2017) 1700081.
[16] K. Liao, P. Mao, N. Li, M. Han, J. Yi, P. He, Y. Sun, H. Zhou, Stabilization of polysulfides via lithium bonds for Li–S batteries, J. Mater. Chem. A 4 (2016) 5406–5409.
[17] Q. Pang, L.F. Nazar, Long-Life and High-Areal-Capacity Li−S Batteries Enabled by a Light-Weight Polar Host with Intrinsic Polysulfide Adsorption, ACS Nano 10 (2016) 4111-4118.
[18] J. Liu, W. Li, L. Duan, X. Li, L. Ji, Z. Geng, K. Huang, L. Lu, L. Zhou, Z. Liu, W. Chen, L. Liu, S. Feng, Y. Zhang, A Graphene-like Oxygenated Carbon Nitride Material for Improved Cycle-Life Lithium/Sulfur Batteries, Nano lett. 15 (2015) 5137-5142.
[19] X. Liang, C. Hart, Q. Pang, A. Garsuch, T. Weiss, L.F. Nazar, A highly efficient polysulfide mediator for lithium–sulfur batteries, Nat. Commun. 6 (2015) 5682.
[20] L. Ni, Z. Wu, G. Zhao, C. Sun, C. Zhou, X. Gong, G. Diao, Core–Shell Structure and Interaction Mechanism of γ-MnO_2 Coated Sulfur for Improved Lithium-Sulfur Batteries, Small 13 (2017) 1603466.
[21] T. Lei, Y. Xie, X. Wang, S. Miao, J. Xiong, C. Yan, TiO_2 Feather Duster as Effective Polysulfides Restrictor for Enhanced Electrochemical Kinetics in Lithium–Sulfur Batteries, Small 13 (2017) 1701013.
[22] M. Yu, J. Ma, H. Song, A. Wang, F. Tian, Y. Wang, H. Qiu, R. Wang, Atomic layer deposited TiO_2 on a nitrogen-doped graphene/sulfur electrode for high performance lithium–sulfur batteries, Energy Environ. Sci. 9 (2016) 1495-1503.

[23] J.-Y. Hwang, H.M. Kim, S.-K. Lee, J.-H. Lee, A. Abouimrane, M.A. Khaleel, I. Belharouak, A. Manthiram, Y.-K. Sun, High-Energy, High-Rate, Lithium–Sulfur Batteries: Synergetic Effect of Hollow TiO_2-Webbed Carbon Nanotubes and a Dual Functional Carbon-Paper Interlayer, Adv. Energy Mater. 6 (2016) 1501480.
[24] T. Zhao, Y. Ye, C.Y. Lao, G. Divitini, P.R. Coxon, X. Peng, X. He, H.K. Kim, K. Xi, C. Ducati, R. Chen, Y. Liu, S. Ramakrishna, R.V. Kumar, A Praline-Like Flexible Interlayer with Highly Mounted Polysulfide Anchors for Lithium–Sulfur Batteries, Small 13 (2017) 1700357.
[25] S. Mei, C.J. Jafta, I. Lauermann, Q. Ran, M. Kärgell, M. Ballauff, Y. Lu, Porous Ti_4O_7 Particles with Interconnected-Pore Structure as a High-Efficiency Polysulfide Mediator for Lithium–Sulfur Batteries, Adv. Funct. Mater. 27 (2017) 1701176.
[26] Q. Pang, D. Kundu, M. Cuisinier, L.F. Nazar, Surface-enhanced redox chemistry of polysulphides on a metallic and polar host for lithium-sulphur batteries, Nat. Commun. 5 (2014) 4759.
[27] H. Wei, E.F. Rodriguez, A.S. Best, A.F. Hollenkamp, D. Chen, R.A. Caruso, Chemical Bonding and Physical Trapping of Sulfur in Mesoporous Magnéli Ti_4O_7 Microspheres for High-Performance Li–S Battery, Adv. Energy Mater. 7 (2017) 1601616.
[28] L. Ma, R. Chen, G. Zhu, Y. Hu, Y. Wang, T. Chen, J. Liu, Z. Jin, Cerium Oxide Nanocrystal Embedded Bimodal Micromesoporous Nitrogen-Rich Carbon Nanospheres as Effective Sulfur Host for Lithium−Sulfur Batteries, ACS Nano 11 (2017) 7274-7283.
[29] R. Fang, S. Zhao, Z. Sun, D.-W. Wang, R. Amal, S. Wang, H.-M. Cheng, F. Li, Polysulfide immobilization and conversion on a conductive polar MoC@MoO_x material for lithium-sulfur batteries, Energy Storage Mater. 10 (2018) 56-61.
[30] L. Kong, X. Chen, B.Q. Li, H.J. Peng, J.Q. Huang, J. Xie, Q. Zhang, A Bifunctional Perovskite Promoter for Polysulfide Regulation toward Stable Lithium–Sulfur Batteries, Adv. Mater. 30 (2018) 1705219.
[31] Z. Hao, R. Zeng, L. Yuan, Q. Bing, J. Liu, J. Xiang, Y. Huang, Perovskite $La_{0.6}Sr_{0.4}CoO_{3-\delta}$ as a new polysulfide immobilizer for high-energy lithium-sulfur batteries, Nano Energy 40 (2017) 360-368.
[32] Z.A. Ghazi, X. He, A.M. Khattak, N.A. Khan, B. Liang, A. Iqbal, J. Wang, H. Sin, L. Li, Z. Tang, MoS_2/Celgard Separator as Efficient Polysulfide Barrier for Long-Life Lithium–Sulfur Batteries, Adv. Mater. 29 (2017) 1606817.

[33] T. Chen, L. Ma, B. Cheng, R. Chen, Y. Hu, G. Zhu, Y. Wang, J. Liang, Z. Tie, J. Liu, Z. Jin, Metallic and polar Co_9S_8 inlaid carbon hollow nanopolyhedra as efficient polysulfide mediator for lithium−sulfur batteries, Nano Energy 38 (2017) 239-248.
[34] J. Pu, Z. Shen, J. Zheng, W. Wu, C. Zhu, Q. Zhou, H. Zhang, F. Pan, Multifunctional Co_3S_4@sulfur nanotubes for enhanced lithium-sulfur battery performance, Nano Energy 37 (2017) 7-14.
[35] T. Chen, Z. Zhang, B. Cheng, R. Chen, Y. Hu, L. Ma, G. Zhu, J. Liu, Z. Jin, Self-Templated Formation of Interlaced Carbon Nanotubes Threaded Hollow Co_3S_4 Nanoboxes for High-Rate and Heat-Resistant Lithium−Sulfur Batteries, J. Am. Chem. Soc. 139 (2017) 12710-12715.
[36] Z. Liu, X. Zheng, S.-l. Luo, S.-q. Xu, N.-y. Yuan, J.-n. Ding, High performance Li–S battery based on amorphous NiS_2 as the host material for the S cathode, J. Mater. Chem. A 4 (2016) 13395-13399.
[37] L. Ma, S. Wei, H.L. Zhuang, K.E. Hendrickson, R.G. Hennig, L.A. Archer, Hybrid cathode architectures for lithium batteries based on TiS_2 and sulfur, J. Mater. Chem. A 3 (2015) 19857-19866.
[38] X. Li, Y. Lu, Z. Hou, W. Zhang, Y. Zhu, Y. Qian, J. Liang, Y. Qian, SnS_2- Compared to SnO_2-Stabilized S/C Composites toward High-Performance Lithium Sulfur Batteries, ACS Appl. Mater. Interfaces 8 (2016) 19550-19557.
[39] J. Park, B.-C. Yu, J.S. Park, J.W. Choi, C. Kim, Y.-E. Sung, J.B. Goodenough, Tungsten Disulfide Catalysts Supported on a Carbon Cloth Interlayer for High Performance Li–S Battery, Adv. Energy Mater. 7 (2017) 1602567.
[40] A. Paolella, D. Laul, V. Timoshevskii, W. Zhu, S. Marras, G. Bertoni, A.S. Wahba, G. Girard, C. Gagnon, L. Rodrigue, B. Commarieu, A. Guerfi, R. Gauvin, M.L. Trudeau, A. Vijh, M. Armand, K. Zaghib, The Role of Metal Disulfide Interlayer in Li−S Batteries, J. Phys. Chem. Lett. 122 (2017) 1014-1023.
[41] G. Babu, N. Masurkar, H. Al Salem, L.M. Arava, Transition Metal Dichalcogenide Atomic Layers for Lithium Polysulfides Electrocatalysis, J. Am. Chem. Soc. 139 (2017) 171-178.
[42] H. Al Salem, G. Babu, C.V. Rao, L.M. Arava, Electrocatalytic Polysulfide Traps for Controlling Redox Shuttle Process of Li−S Batteries, J. Am. Chem. Soc. 137 (2015) 11542-11545.

[43] D. Liu, C. Zhang, G. Zhou, W. Lv, G. Ling, L. Zhi, Q.H. Yang, Catalytic Effects in Lithium–Sulfur Batteries: Promoted Sulfur Transformation and Reduced Shuttle Effect, Adv. Sci. 5 (2018) 1700270.
[44] G. Zhou, H. Tian, Y. Jina, X. Tao, B. Liu, R. Zhang, Z.W. Seh, D. Zhuo, Y. Liu, J. Sun, J. Zhao, C. Zu, D.S. Wu, Q. Zhang, Y. Cui, Catalytic oxidation of Li_2S on the surface of metal sulfides for Li−S batteries, Proc. Natl. Acad. Sci. USA 114 (2017) 840-845.
[45] Z. Gao, Y. Zhang, N. Song, X. Li, Towards flexible lithium-sulfur battery from natural cotton textile, Electrochim. Acta 246 (2017) 507–516.
[46] Z. Gao, Y. Schwab, Y. Zhang, N. Song, X. Li, Ferromagnetic Nanoparticle–Assisted Polysulfide Trapping for Enhanced Lithium–Sulfur Batteries, Adv. Funct. Mater. 28 (2018) 1800563.
[47] Y. Zhang, Z. Gao, X. Li, Capillarity Composited Recycled Paper/Graphene Scaffold for Lithium–Sulfur Batteries with Enhanced Capacity and Extended Lifespan, Small 13 (2017) 1701927.
[48] T. Lei, W. Chen, J. Huang, C. Yan, H. Sun, C. Wang, W. Zhang, Y. Li, J. Xiong, Multi-Functional Layered WS_2 Nanosheets for Enhancing the Performance of Lithium–Sulfur Batteries, Adv. Energy Mater. 7 (2017) 1601843.
[49] M. Nagai, K. Koizumi, S. Omi, NH_3-TPD and XPS studies of Ru/Al_2O_3 catalyst and HDS activity, Catal. Today 35 (1997) 393–405.
[50] A. Infantes-Molina, A. Romero-Pérez, E. Finocchio, G. Busca, A. Jiménez-López, E. Rodríguez-Castellón, HDS and HDN on SBA-supported RuS_2 catalysts promoted by Pt and Ir, J. Catal. 305 (2013) 101-117.
[51] A. Lewera, J. Inukai, W.P. Zhou, D. Cao, H.T. Duong, N. Alonso-Vante, A. Wieckowski, Chalcogenide oxygen reduction reaction catalysis: X-ray photoelectron spectroscopy with Ru, Ru/Se and Ru/S samples emersed from aqueous media, Electrochim. Acta 52 (2007) 5759-5765.
[52] A. Romero-Pérez, A. Infantes-Molina, E. Rodríguez-Castellón, A. Jiménez-López, SBA-15 type materials as support of catalysts based on ruthenium sulfide for sulfur removal, Appl. Catal. B: Environ. 97 (2010) 257-268.
[53] C. Zhang, Y. Lin, J. Liu, Sulfur double locked by a macro-structural cathode and a solid polymer electrolyte for lithium–sulfur batteries, J. Mater. Chem. A 3 (2015) 10760-10766.

[54] W. Ni, S. Liu, Y. Fei, Y. He, X. Ma, L. Lu, Y. Deng, CoO@Co and N-doped mesoporous carbon composites derived from ionic liquids as cathode catalysts for rechargeable lithium–oxygen batteries, J. Mater. Chem. A 4 (2016) 7746-7753.
[55] R.R. Rao, M.J. Kolb, N.B. Halck, A.F. Pedersen, A. Mehta, H. You, K.A. Stoerzinger, Z. Feng, H.A. Hansen, H. Zhou, L. Giordano, J. Rossmeisl, T. Vegge, I. Chorkendorff, I.E.L. Stephens, Y. Shao-Horn, Towards identifying the active sites on RuO_2(110) in catalyzing oxygen evolution, Energy Environ. Sci. 10 (2017) 2626-2637.
[56] J. Balach, T. Jaumann, S. Muhlenhoff, E. J., L. Giebeler, Enhanced polysulphide redox reaction using a RuO_2 nanoparticle-decorated mesoporous carbon as functional separator coating for advanced lithium–sulphur batteries, Chem. Commun. 52 (2016) 8134-8137.
[57] K. Liao, X. Wang, Y. Sun, D. Tang, M. Han, P. He, X. Jiang, T. Zhang, H. Zhou, An oxygen cathode with stable full discharge–charge capability based on 2D conducting oxide, Energy Environ. Sci. 8 (2015) 1992-1997.

Figures：

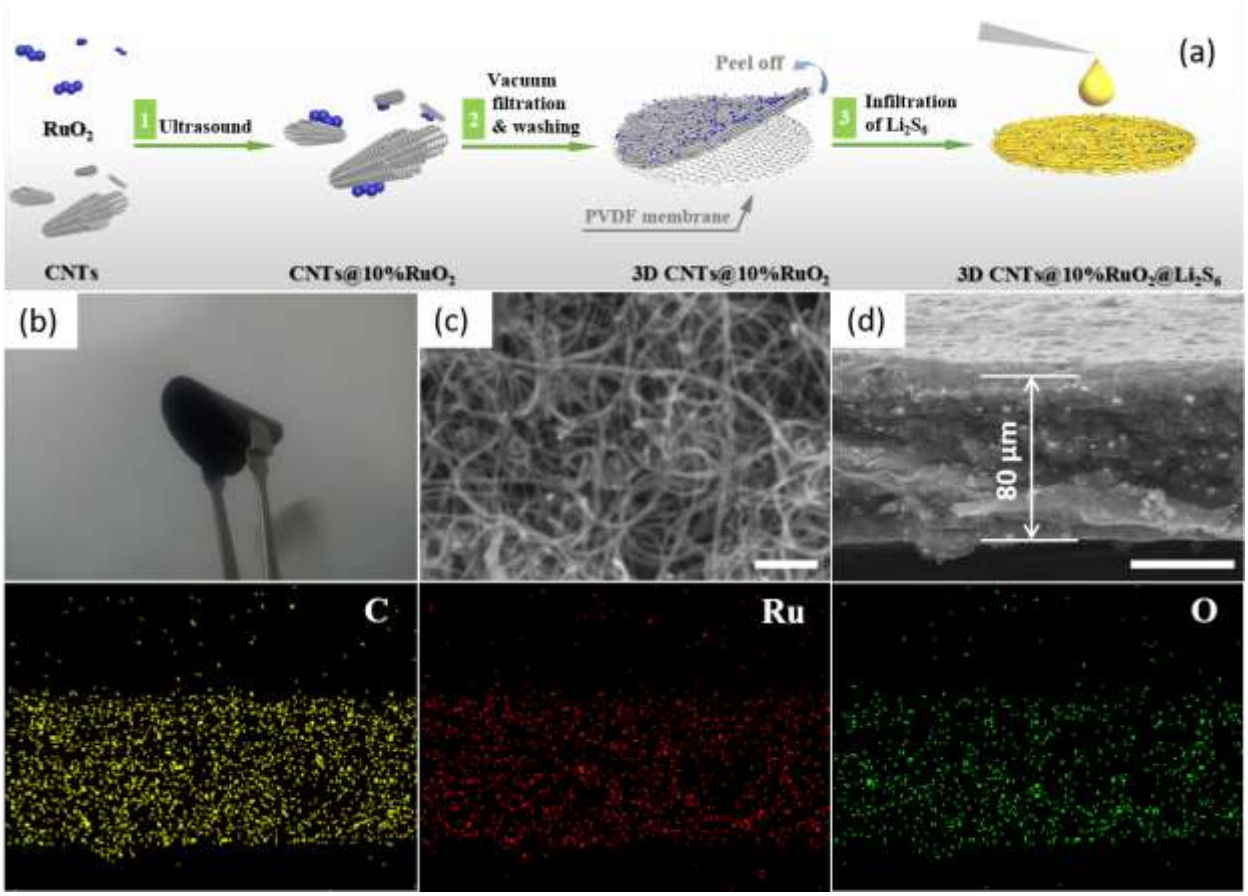

Fig. 1

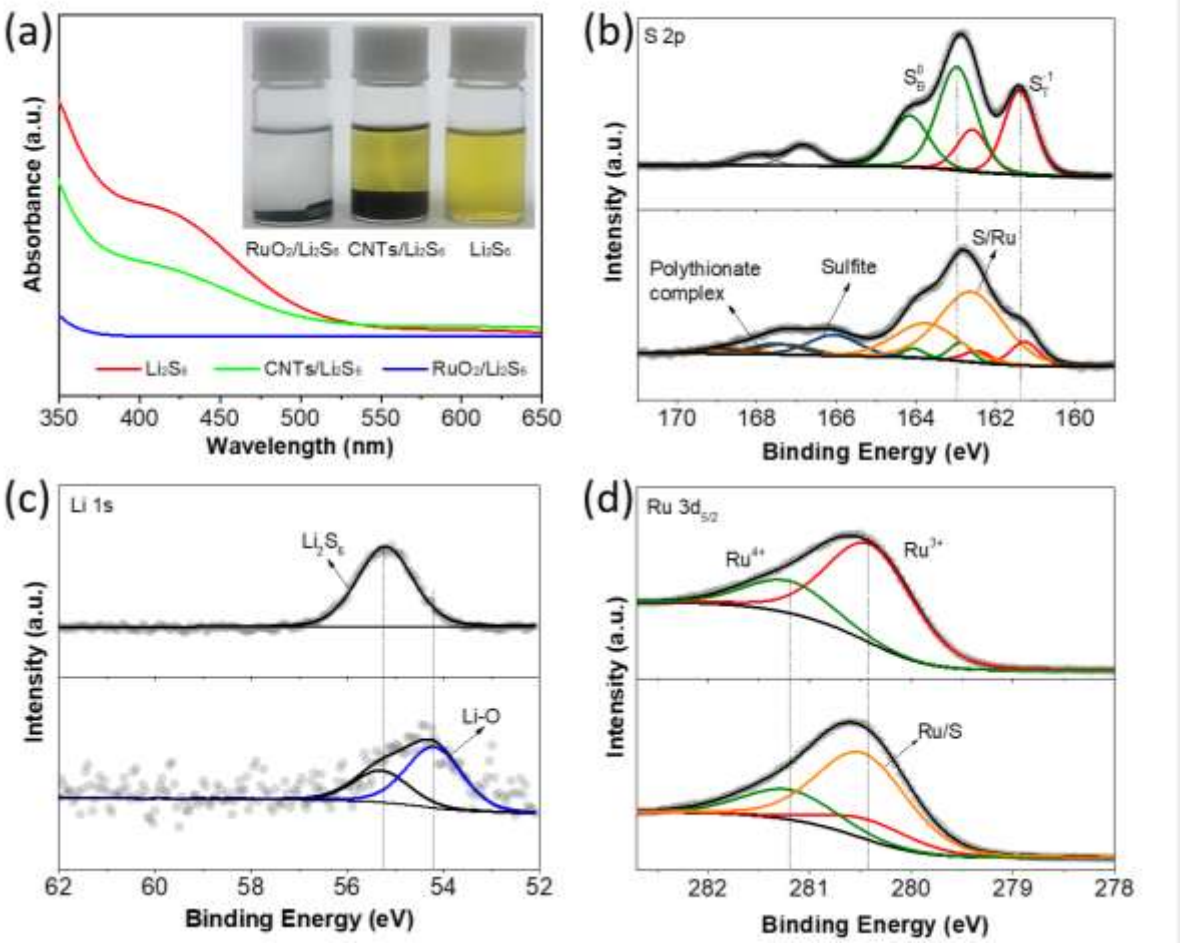
(a)
Absorbance (a.u.)
RuO2/Li2S6 CNTs/Li2S6 Li2S6
Li2S6
CNTs/Li2S6
RuO2/Li2S6
350 400 450 500 550 600 650
Wavelength (nm)
(b)
S 2p
Intensity (a.u.)
Polythionate complex
Sulfite
S/Ru
170 168 166 164 162 160
Binding Energy (eV)
(c)
Li 1s
Li2S6
Li-O
Intensity (a.u.)
62 60 58 56 54 52
Binding Energy (eV)
(d)
Ru 3d5/2
Ru4+
Ru3+
Ru/S
Intensity (a.u.)
282 281 280 279 278
Binding Energy (eV)

Fig. 2

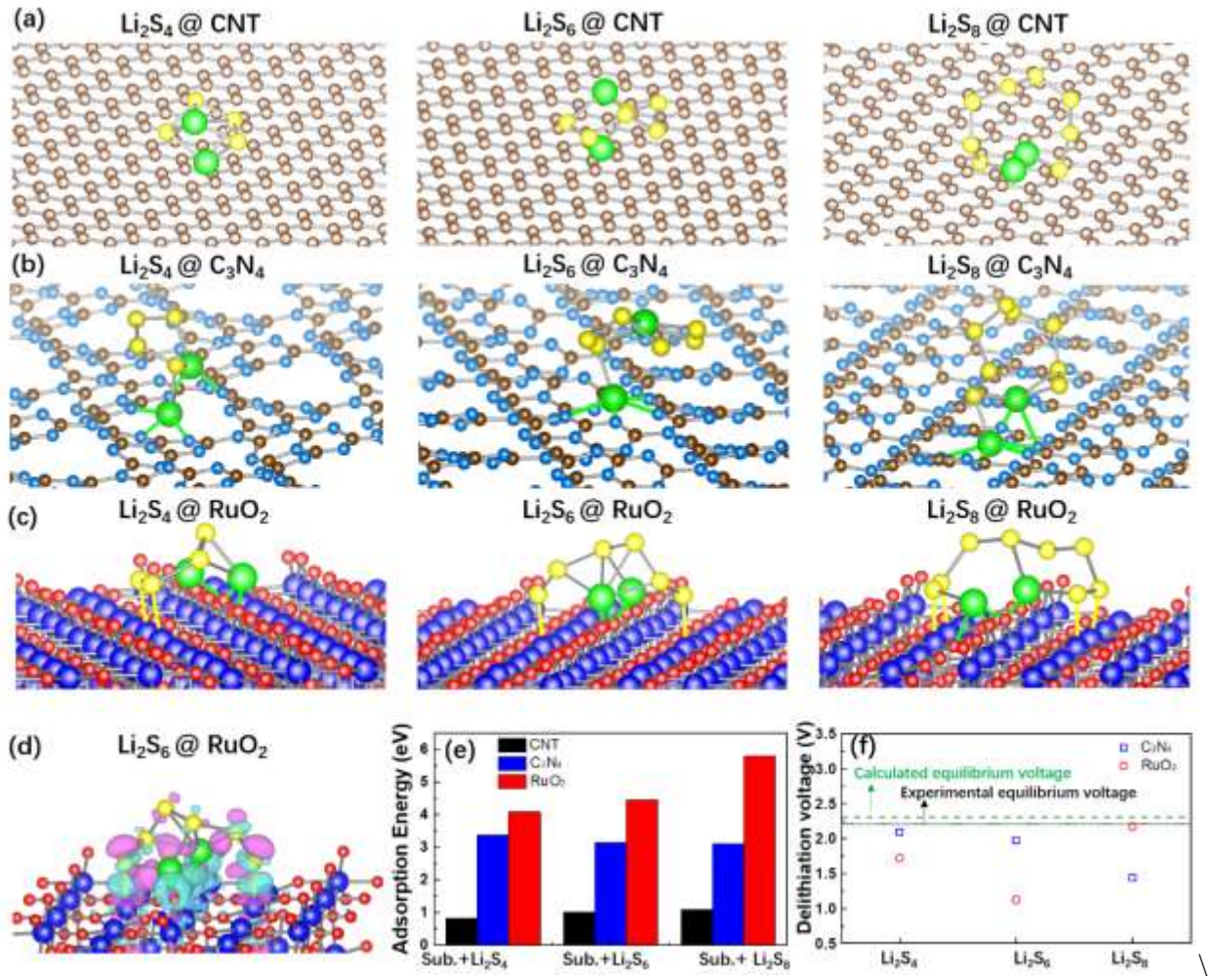
(a)
Li2S4 @ CNT
Li2S6 @ CNT
Li2S8 @ CNT
(b)
Li2S4 @ C3N4
Li2S6 @ C3N4
Li2S8 @ C3N4
(c)
Li2S4 @ RuO2
Li2S6 @ RuO2
Li2S8 @ RuO2
(d)
Li2S6 @ RuO2
(e)
CNT
C3N4
RuO2
Adsorption Energy (eV)
Sub.+Li2S4
Sub.+Li2S6
Sub.+ Li2S8
(f)
C3N4
RuO2
Calculated equilibrium voltage
Experimental equilibrium voltage
Delithiation voltage (V)
Li2S4
Li2S6
Li2S8

Fig. 3

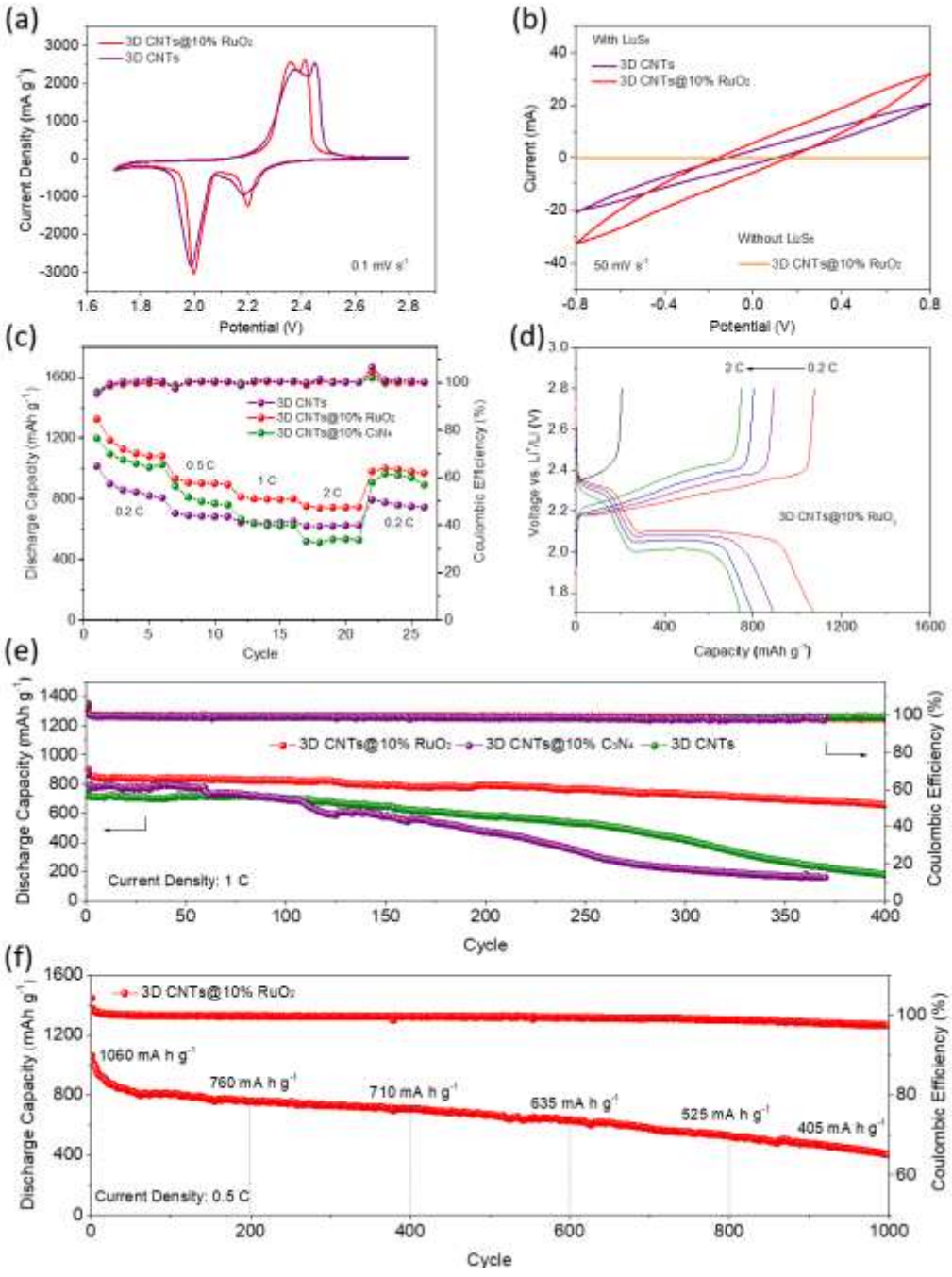
(a)
3D CNTs@10% RuO2
3D CNTs
Current Density (mA g-1)
Potential (V)
0.1 mV s-1
(b)
With Li2Se
3D CNTs
3D CNTs@10% RuO2
Current (mA)
Potential (V)
Without Li2Se
50 mV s-1
3D CNTs@10% RuO2
(c)
3D CNTs
3D CNTs@10% RuO2
3D CNTs@10% C3N4
Discharge Capacity (mAh g-1)
Coulombic Efficiency (%)
Cycle
0.5 C
1 C
2 C
0.2 C
0.2 C
(d)
2 C
0.2 C
Voltage vs. Li+/Li (V)
3D CNTs@10% RuO2
Capacity (mAh g-1)
(e)
3D CNTs@10% RuO2
3D CNTs@10% C3N4
3D CNTs
Discharge Capacity (mAh g-1)
Coulombic Efficiency (%)
Current Density: 1 C
Cycle
(f)
3D CNTs@10% RuO2
1060 mA h g-1
760 mA h g-1
710 mA h g-1
635 mA h g-1
525 mA h g-1
405 mA h g-1
Discharge Capacity (mAh g-1)
Coulombic Efficiency (%)
Current Density: 0.5 C
Cycle

Fig. 4

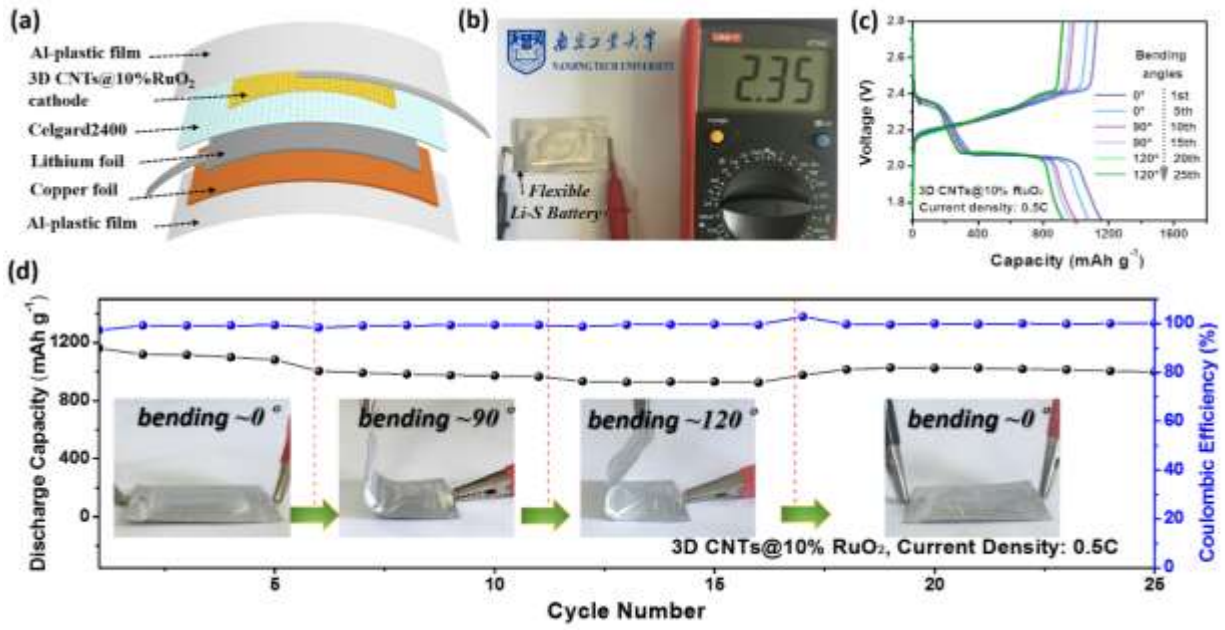
(a)
Al-plastic film
3D CNTs@10%RuO2
cathode
Celgard2400
Lithium foil
Copper foil
Al-plastic film
(b)
Flexible
Li-S Battery
(c)
Voltage (V)
Capacity (mAh g-1)
Bending angles
3D CNTs@10% RuO2
Current density: 0.5C
(d)
Discharge Capacity (mAh g-1)
Coulombic Efficiency (%)
Cycle Number
bending ~0 °
bending ~90 °
bending ~120 °
bending ~0 °
3D CNTs@10% RuO2, Current Density: 0.5C

Fig. 5

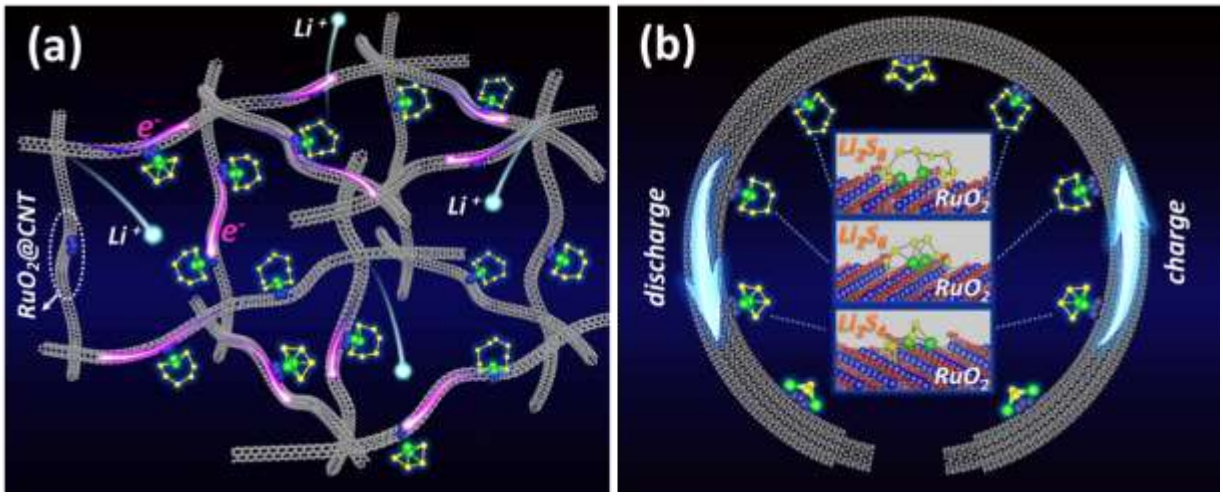
(a)
Li+
e-
Li+
e-
Li+
RuO2@CNT
(b)
discharge
charge
Li2S8
Li2S6
Li2S4
RuO2
RuO2
RuO2

Fig. 6

Figure captions：

Fig. 1. (a) Illustrated formation procedures of the freestanding 3D CNTs@10%RuO_2 electrode; (b) digital photo of 3D CNTs@10%RuO_2 film under the 180° bending condition; (c) the SEM image from surface view of the 3D CNTs@10%RuO_2 film, and the scale bar is 200 nm; (d) cross-sectional SEM image of the 3D CNTs@10%RuO_2 and corresponding EDX mapping of C, Ru and O elements in the bottom, the scale bar is 50 μm.

Fig. 2. (a) UV-vis spectra of the blank Li_2S_6 solution or Li_2S_6 solution after immersed with the same surface area of RuO_2 and CNTs (inset image of the Li_2S_6 solution with different absorbing materials); (b, c) Elemental XPS spectra of Li_2S_6 (upper) before and after exposure to RuO_2 (bottom): (b) S2p; (c) Li1s; and (d) $Ru3d_{5/2}$ XPS spectra of RuO_2 (upper) and RuO_2@Li_2S_6 (bottom).

Fig. 3. (a) Optimization of polysulfides (Li_2S_4, Li_2S_6, and Li_2S_8) on (a) graphene, (b) g-C_3N_4, and (c) RuO_2 (110) surface; (d) Charge difference after Li_2S_6 adsorbed on RuO_2 (110) surface. Light blue: electron gain, pink: electron loss; (e) the calculated adsorption energy for different adsorbate (RuO_2, C_3N_4, and CNTs) with different polysulfides (Li_2S_4, Li_2S_6 and Li_2S_8); (f) the delithiation voltage after forming the adsorption conformations for RuO_2 and g-C_3N_4. Olive dashed line: calculated equilibrium voltage of $2Li + S \rightarrow Li_2S$, and black dotted line: experimental voltage (average value) of the Li-S battery.

Fig. 4. (a) The first CV curve of the Li-S batteires with the 3D CNTs and 3D CNTs@10%RuO_2 electrodes at a scan rate of 0.1 mV s^{-1}; (b) polarization curves of both electrodes recorded at 50 mV s^{-1}; (c) rate performance and Coulombic efficiency of the Li-S batteries with 3D CNTs, 3D CNTs@10%C_3N_4, and 3D CNTs@10%RuO_2 electrodes at varied current rates with a sulfur-loading of 2 mg cm^{-2} and their corresponding charge-discharge curves (d); (e) comparision of the cycling stability and coulombic efficiency of the Li-S batteries with the 3D CNTs, 3D CNTs@10%C_3N_4, and 3D CNTs@10%RuO_2 electrodes at 1 C rate; (f) long cycling performance and coulombic efficiency of the Li-S battery with the 3D CNTs@10%RuO_2 electrode at 0.5 C rate.

Fig. 5. (a) Schematic representation and (b) digital photograph of the flexible Li-S battery, an open circuit voltage of 2.35 V is demonstrated after assembling; (c) charge-discharge curves of the flexible Li-S battery with the 3D CNTs@10%RuO_2 cathode at various bending angles (0 °, 90 °, and 120 °) for the first and 5th cycle; (c) cycling stability and coulombic efficiency of flexible Li-S battery at 0.5 C, and the inset Fig.s correspond to the bending state during the test.

Fig. 6. Schematic illustration of the conversion process and interaction of polysulfides with the RuO_2 nanoparticles in the freestanding 3D CNTs@10%RuO_2 composite. The two-phase interfacial reaction is confined by both the anchored polysulfides and electronic transport in entire cathode.